Density-functional theory approach to ultrafast laser excitation of semiconductors: Application to the A_1 phonon in tellurium

P. Tangney[1] and S. Fahy[2]
[1]*International School for Advanced Studies, via Beirut 2-4, 34013 Trieste, Italy*
[2]*Department of Physics, University College, Cork, Ireland*
(Received 15 August 2001; published 9 January 2002)

Calculations of the A_1 phonon frequency in photoexcited tellurium are presented. The phonon frequency as a function of photoexcited carrier density and phonon amplitude is determined, including anharmonic effects. The sensitivity of the A_1 mode to photoexcitation is related to the Peierls mechanism for stabilizing the α-Te structure. The assumptions of slow and fast carrier recombination are investigated and it is found that the two regimes give qualitatively different predictions for the excitation dependence of the phonon frequency. Recent pump-probe experiments are compared with the calculations. The predictions based on fast carrier recombination are not in agreement with experiment. The reflectivity oscillations expected to occur in pump-probe experiments are simulated, including the coupled effects of optical absorption, carrier diffusion, and phonon dynamics. Using the calculated dependence of phonon frequency on carrier density (assuming slow carrier recombination) and experimental values for the optical dielectric constants, the derivative of the frequency peak for reflectivity oscillations with respect to pump fluence is found to be -0.085 THz per mJ/cm^2, compared to an experimental value of -0.07 THz per mJ/cm^2 in the low-fluence regime. The ambipolar diffusion constant for the optically excited carriers is estimated to be 10 cm^2/s, substantially smaller than its equilibrium value. The effects of carrier diffusion are found to be more important than phonon anharmonicity in the observed changes of phonon frequency within the first few cycles of motion after laser excitation. Greatly increased damping of the reflectivity oscillations at high pump fluences, which was reported in recent experiments, is not found in the simulations.

DOI: 10.1103/PhysRevB.65.054302 PACS number(s): 78.20.Bh, 78.47.+p, 71.15.Pd, 71.15.Nc

I. INTRODUCTION

Due to rapid improvements in laser technology and the ability to produce very short ($\sim$10–100 fs) and powerful ($\sim$1–10 mJ/cm^2) laser pulses, there is increasing need for theoretical insight into the interactions of such laser pulses with matter.[1] Experiments using powerful laser pulses of duration much shorter than phonon periods are now feasible and direct, time-domain studies of phonon motion are possible with pump-probe techniques.[2] For the duration of application of such a laser pulse, its electromagnetic field generates a coherent superposition of excited electron and hole states in the material. However, coherence is quickly lost and, on the time scales of interest in phonon motion, the primary effect of such a laser pulse (when the photon energy is sufficiently large to generate real electron-hole pairs) is to instantaneously prepare the sample with an excited distribution of electrons within the bands.

Altering the electron distribution in this way changes the forces between ions and the effective potential energy landscape experienced by each ion. Since electrons are excited out of bonding states, the energy barriers between stable and metastable high-symmetry crystalline structures are usually lowered and their relative stability may be changed. In materials which possess A_1 phonon modes, any change in the distribution of electrons (e.g., by laser pulse excitation) can change the equilibrium positions of the ions. In such materials, the equilibrium positions of the atoms within each unit cell are not determined solely by crystal symmetry, but are specified by one or more free parameters. The excitation of an A_1 mode corresponds to a time variation of these parameters.

Thus, a very short laser pulse may be used to instantaneously place ions out of equilibrium. The ions then oscillate about their new equilibrium positions, starting with zero velocity immediately after the pulse, producing a phonon motion with a cosinelike time dependence. This mechanism is known as ''displacive excitation of coherent phonons'' (DECP).[3] [This is in contrast to a sinelike time dependence which results if a velocity impulse is imparted to the ions through second-order Raman coupling to the laser radiation,[2,5] without any change in their equilibrium positions — a mechanism known as impulsive stimulated Raman scattering (ISRS).] If the excitation of electrons is homogeneous in the material, only zone-center modes can be excited. Such excitation of the phonon motion can be detected by measuring oscillations in the optical reflectivity of the material using a probe pulse, delayed with respect to the exciting pump pulse.[2]

In crystals without an A_1 mode, the weakening of bond strengths by electronic excitation will usually lower the energy barriers between distinct crystalline phases without changing the equilibrium ion positions in the preexisting phase. However, when the excitation is strong enough, structural stability may be lost, leading to a structural transition — a mechanism known as ''plasma annealing.''[4,6–9]

Density functional theory[10] (DFT) has provided a framework within which calculations of many physical properties have been successfully performed.[11–13] In this paper we use DFT methods to calculate the effect of short-time-scale elec-

tronic excitation on the A_1 phonon frequency of tellurium, with a view to interpreting the results of recent femtosecond pump-probe experiments and demonstrating clearly the mechanism by which laser-induced changes in electronic structure can alter ion dynamics. In particular, we will compare with the results of recent pump-probe spectroscopic experiments on tellurium,[15,16] which observed large amplitude phonons of A_1 symmetry following short-time-scale laser excitation and measured a linear decrease of the frequencies of these oscillations with pump fluence. We have discussed qualitative comparisons with experiment previously.[17] Here we introduce a full model of the reflectivity oscillations in the low-fluence regime and compare the results quantitatively with experiment.

Our use of DFT methods is not entirely within the formal structure of density functional theory. In order to appropriately represent the electronic relaxation time scales in the laser excitation (in particular, the relatively slow electron-hole recombination), we use a constrained form of DFT, where occupations of specific classes of orbitals are kept fixed.[18] Our approach is discussed in detail in Sec. IV and the results obtained are compared in Sec. VII with those found using finite-temperature DFT (Ref. 14) to represent the excited electron-hole plasma. A number of previous calculations[7–9] have used the finite-temperature approach to study mode softening and plasma annealing in other semiconductors. From a theoretical point of view, a major conclusion of this paper is the qualitative difference between the results on mode softening in tellurium obtained using a fixed electron-hole density and those obtained using a fixed high temperature. This conclusion has general implications for the use of excited-state electron distributions in the simulation of ion dynamics.

The rest of this paper is organized as follows: In Sec. II, we discuss the relevant time scales for relaxation of the laser-induced, excited electronic state of the material. We discuss the crystal structure of Te in Sec. III, highlighting the role of the Peierls mechanism for stabilization of the α-Te structure and the relevance of this mechanism to the A_1 mode. Details of the scheme for constrained occupation of conduction and valence bands are presented in Sec. IV. The frozen phonon approach and the calculation of structural energies are discussed in Secs. V and VI, respectively. In Sec. VII, we present the main results of our calculations for the A_1 mode softening in Te. Section VIII introduces a model of coupled electromagnetic radiation, carrier diffusion, and phonon dynamics to simulate the expected pump-probe reflectivity oscillations in tellurium. The results are compared in detail with experimental results in Refs. 15 and 16. Finally, in Sec. IX, we present our overall conclusions.

II. RELAXATION TIME SCALES

When a very short ($\lesssim$100 fs) laser pulse, with photon energy larger than the direct band gap, is incident on a semiconductor crystal, electrons are excited into conduction bands, creating electron-hole pairs. The semiconductor then undergoes several temporarily overlapping stages of relaxation before it returns once again to thermodynamic equilibrium. When attempting to model such a system, it is important to be aware of the time scales of the various relaxation processes. We will be concerned with those processes which occur within a few periods of the tellurium A_1 phonon frequency, i.e., times $<1-2$ ps.

During application of the exciting laser pulse, coherent superposition of excited electronic states gives rise to an electrical polarization of the medium. Once the laser pulse is no longer present, this coherence is lost, typically on a time scale of 100 fs at low and moderate levels of excitation or substantially less in highly excited materials, leaving an incoherent distribution of excited electron-hole pairs. Experiments suggest that carriers within a given subband thermalize among themselves very quickly[19] (in much less than 100 fs) at the very high densities of excited electrons considered here, but that intervalley scattering may be considerably slower ($\sim$ ps).[1] In this paper we will not be directly concerned with these relaxation processes, except insofar as we assume that they occur relatively quickly and establish a thermal distribution of carriers within individual bands. We will assume thermal (Fermi-Dirac) distributions within each band. For incident photons of energy 1.5 eV, we would expect the initial carrier temperature for electrons and holes to be approximately 0.4 eV. However, as we shall see in Sec. VI, the exact distribution of electrons within the conduction-band states (and holes among the valence bands) is not crucial to the A_1 phonon frequency. Thus, carrier cooling, which may occur very rapidly (e.g., by phonon emission), does not strongly affect the dynamics of the A_1 phonon.

In general, the electrons in the conduction band and the holes in the valence band are initially at different temperatures but electron-hole scattering typically establishes a common temperature in times of the order of a picosecond. For the high carrier densities of interest here, this equilibration is likely to occur in substantially less than a picosecond.

In considering the interaction between the photoexcited electron-hole plasma and the phonons, we must distinguish between two types of effect: (a) coherent excitation of the zone-center A_1 mode and (b) random thermal excitation of phonon modes throughout the zone by carrier-phonon scattering. The electron-phonon matrix elements which give rise to (a) are also the source of (b) but the statistical character of the effects is quite different. The forces in (a) give rise to the coherent motion of the ions (the main focus of this study) with an associated change in the energies of electron and hole states, but without any change in the occupations of electronic states. From the point of view of the electronic degrees of freedom, this is an isentropic process. In (b), the excitation of phonons can be viewed as random events, with an associated change in occupation of carrier states and an exchange of entropy between the electronic and vibrational degrees of freedom, leading eventually to the electronic and vibrational temperatures being equal.

At moderate excitation densities ($10^{17}-10^{18}$ cm^{-3}), the carriers reach lattice temperatures in hundreds of picoseconds.[1] This may happen much more quickly (as fast as a few picoseconds) at the relatively high densities considered during the coherent excitation of the A_1 phonon. The transfer of thermal energy is more rapid when the carrier

distribution is in its initial, highly excited nonthermal state, but once the electrons are thermalized within a given subband, the rates of carrier-phonon interactions can be expected to be slower due to the increased probability of occupancy of the final electron state after interaction with a phonon.[1]

As we shall see below, from the point of view of its effects on the A_1 phonon in tellurium, the most important aspect of carrier-phonon scattering is that it does not change the total electron-hole density. Moreover, double-pulse excitation experiments, where the delay between two pulses is sufficient to allow the lattice to heat after the first pulse, show that the effect of lattice heating on the A_1 phonon frequency is small[15] for this system.

A crucial issue for modeling the ion dynamics is the time scale for carrier recombination. In general, for moderate excitation densities, the time scale for electrons and holes to reach a chemical equilibrium is of the order of nanoseconds.[1] At the very high excitation densities considered here, this rate may be enhanced[20] and this has been the assumption in previous theoretical investigations of photoexcitation of semiconductors by ultrashort laser pulses.[8,9] The experiments of Hunsche *et al.*[15] on tellurium show no significant change in the A_1 phonon lifetime as the electron-hole plasma density is altered, as would be the case if electron-hole recombination occurred on a time scale comparable to the phonon period. (Relaxation of electronic or rotational degrees of freedom on a time scale comparable to the period of a vibrational mode leads to dissipation of energy from the mode.[21]) Thus, we consider two possible scenarios.

(i) Slow electron-hole recombination: then the number of electrons in the conduction band remains constant during the phonon motion (disregarding diffusion effects for the moment — see Sec. VIII). As discussed above, the relaxation of the carrier distribution within individual bands (conduction and valence) is fast and so *the electronic system can be characterized by two separate thermal carrier distributions, electrons in the conduction bands and holes in the valence bands, each characterized by a different chemical potential and a temperature substantially higher than the lattice temperature.*

(ii) Fast electron-hole recombination: throughout the phonon motion chemical equilibrium is maintained between carriers in the valence and conduction bands and, at each point of the motion, *the entire carrier distribution (electrons and holes) may be specified by a single chemical potential and a temperature comparable to the band gap.*

The second scenario has been used in previous methods of modeling ultrafast electronic excitation which have been applied to study plasma annealing in different systems (e.g., Si and GaAs).[7–9] They have assumed that the laser excitation can be modeled on the time scale of ionic motion as a very high electronic temperature, with chemical equilibrium between conduction-band and valence-band carriers. In the method of Silvestrelli *et al.*,[9] the carrier temperature is kept constant as the ions move. In the method of Stampfli and Benneman,[8] the entropy of the carriers is kept constant as the ions move.

In this paper we show that results based on slow electron-hole recombination are in good agreement with the excitation experiments for tellurium[15] and that the results from calculations based on a fast recombination rate and constant high temperature give qualitatively different results. We note that the first scenario ignores the problem that intervalley scattering may be slow compared with the phonon period and that one might have several carrier distributions within a given band. However, since the forces driving the A_1 mode are found to depend primarily on the total number of excited electrons in the conduction bands and very little on their exact distribution within the conduction band (see Sec. VI A), it appears that the effect of intervalley relaxation on the phonon frequency is small.

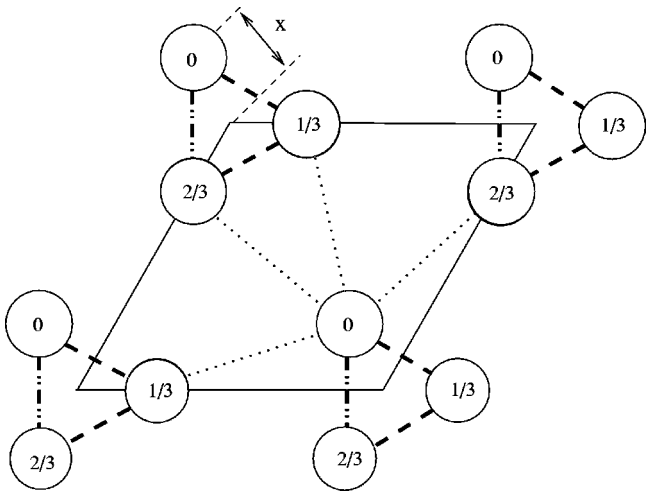

FIG. 1. View of α-Te structure looking down along the c axis. The relative altitudes of the atoms in units of c are as indicated. The dashed lines indicate nearest-neighbor bonds. The dotted lines indicate second-nearest neighbors.

III. STRUCTURE

The stable form of tellurium at low pressure is α-Te (Fig. 1), in which twofold-coordinated tellurium atoms form infinite helical chains parallel to the c axis of the trigonal $P3_121$-D_3^4 structure.[22] The three atoms per unit cell are at $(x0\frac{1}{3}, 0x\frac{2}{3}, \overline{xx}0)$ and form a single, complete turn of a helical chain. Each helix is surrounded by six equidistant helices (three of these are shown in Fig. 1 around the helix on the bottom right of the figure) and each atom has four second-nearest neighbors in these adjacent helices. The atomic position free parameter x is equal to the ratio of the radius of each helix to the interhelical distance. The motion of atoms in the A_1 phonon mode corresponds to a variation of the helical radius x, maintaining the symmetry of the crystal. Since its value is not determined by symmetry, the equilibrium value x_{eq} is therefore sensitive to the precise details of the electronic structure. This allows for an excitation of the A_1 mode within the DECP mechanism since any change in the occupation of electronic states may alter the value of x_{eq}.

At the special value $x=\frac{1}{3}$, the nearest- and second-nearest-neighbor distances become equal, the atomic coordination number increases to six, the helical chain structure is

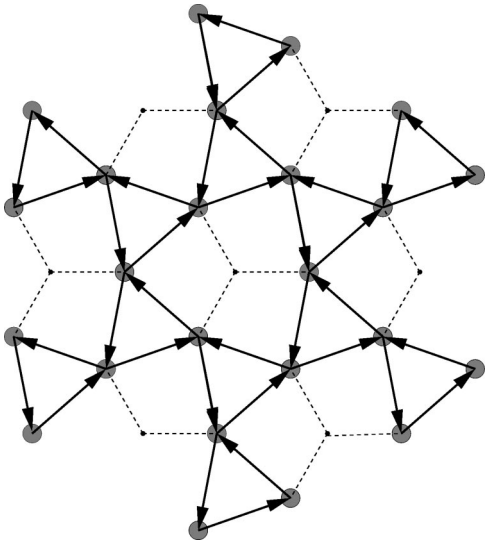

FIG. 2. View of the tellurium structure when $x>\frac{1}{3}$. The dotted lines shown are from the center of each helix formed when $x<\frac{1}{3}$ to the atoms of that helix (see Fig. 1). The arrows connect nearest neighbors and are directed from atoms of lower altitude to atoms of higher altitude.

destroyed, and the structure can be classified as rhombohedral, with space group $R\bar{3}m$-D_{3d}^5 and one atom per unit cell. The high-pressure γ-Te form of tellurium, which is stable above $\sim$70 kbar, has this structure.[22]

The α-Te structure may be viewed as a Peierls distortion of the γ-Te structure. The distortion is a standing wave with wave vector $\mathbf{q}=(2\pi/c)\hat{\mathbf{z}}$ and atomic displacements

$$\delta\mathbf{r}=\left(x-\frac{1}{3}\right)\mathrm{Re}\{(\hat{\mathbf{x}}-i\hat{\mathbf{y}})\exp[i\mathbf{q}\cdot(\mathbf{r}-\mathbf{c}/3)]\},$$

where $\hat{\mathbf{x}}$, $\hat{\mathbf{y}}$, and $\hat{\mathbf{z}}$ are unit vectors in the x, y, and z directions, respectively. When x is increased past $\frac{1}{3}$ the system is fourfold coordinated, the nearest neighbors of each atom being those that were its second-nearest neighbors for $0<x<\frac{1}{3}$. A convenient way of looking at this for our present purposes is that each atom is shared between two different helices (see Fig. 2). At $x=\frac{1}{3}$ each atom has an identical relationship with the helices formed for values of x on either side of $\frac{1}{3}$.

Figures 3(a) and 3(b) show the band structure of Te at $x=x_{eq}=0.2686$ and $x=\frac{1}{3}$, respectively. The experimentally determined lattice constants ($a=4.4561$ Å and $c=5.9271$ Å) have been used in these calculations. Nine valence bands (six electrons per atom) are occupied in the semiconducting equilibrium structure. The higher symmetry of γ-Te is responsible for the high degeneracy of states in Fig. 3(b). It is precisely the energy gained by the splitting of these degeneracies at the Fermi level when x is decreased that leads to the α-Te structure — a striking example of the Peierls mechanism — and the calculated direct band gap (at H) attains approximately its maximum value for the equilibrium value of x. Since the structural stability of the α-Te structure and the value of $x=x_{eq}$ at equilibrium is heavily influenced by the splitting of the conduction and valence

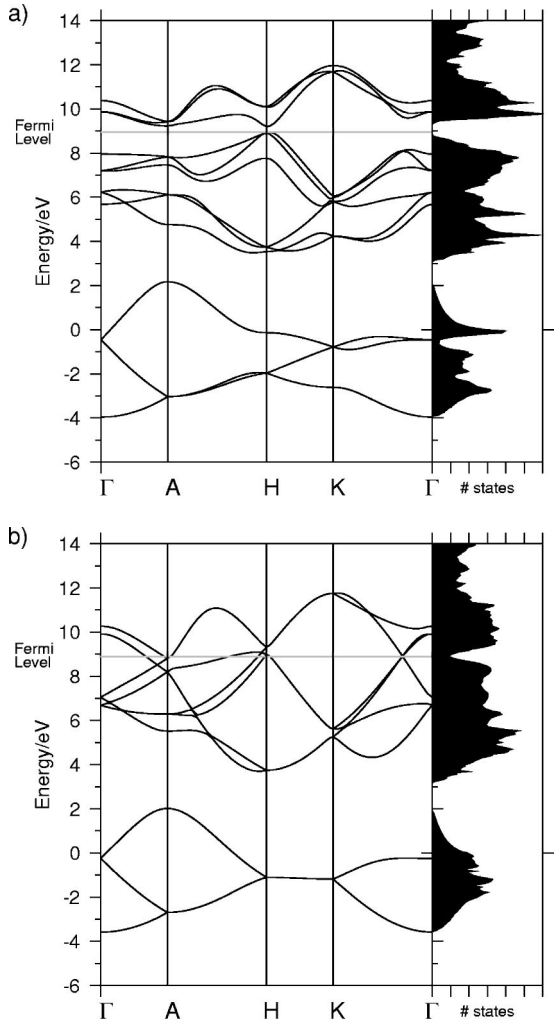

FIG. 3. Calculated band structure and density of states of α-Te at (a) $x=x_{equil}=0.2686$ and (b) $x=\frac{1}{3}$. All bands are threefold degenerate at $x=\frac{1}{3}$.

bands near the Fermi level, the value of x_{eq} is strongly affected by laser excitation of the electron-hole pairs. Thus, we see that the strong DECP of the A_1 phonon is directly related to the Peierls mechanism for stabilizing the α-Te structure.

IV. ENERGY LEVEL FILLING IN BAND STRUCTURE CALCULATIONS

For standard ground-state band structure calculations, electron states are filled strictly in order of increasing energy. However, in this work we are concerned with excited electronic configurations and so the filling of states is not so straightforward. We will investigate two different regimes of electronic relaxation and hence band structure filling, corresponding to two different time scales of the electron-hole recombination rate : (i) where the conduction-band electrons and valence-band holes are in chemical equilibrium (i.e., rapid electron-hole recombination) and hence share a single chemical potential; (ii) where chemical equilibrium between valence-band and conduction-band carriers is not established

(i.e., slow electron-hole recombination) and so they have two separate chemical potentials.

Apart from the unorthodox filling of bands, all other aspects of the band structure and total energy calculations presented here follow the standard self-consistent, plane-wave pseudopotential methods.[24,11]

A. Energy level filling for electrons and holes in chemical equilibrium

Here the number of electrons in the conduction bands is determined solely by the temperature. The energy levels are filled according to the normal, finite-temperature version of DFT: the occupancy w_i of each energy level ϵ_i is given by the Fermi-Dirac distribution with a given temperature T:

$$w_i = \frac{1}{\exp\left[\dfrac{\epsilon_i - \mu}{\tau}\right] + 1},$$

where μ is the chemical potential and $\tau = k_B T$ is the thermal energy. Here the only ''control variable'' in the calculation is the temperature T, the chemical potential being constrained by the requirement of overall charge neutrality (i.e., that the numbers of electrons and holes be equal).

The chemical potential is found by a bisection method as follows: Assuming that it lies within a certain range $[E_1, E_2]$, the Fermi-Dirac distribution is formed and the energy levels filled using $\mu = (E_2 + E_1)/2$. The number of electrons are then counted up, and if there are too few, then this value of μ becomes the new E_1, and if there are too many, then this value of μ becomes E_2. This process is repeated until a value of μ which produces the correct number of electrons is found. The band energies and charge density are calculated self-consistently, based on the occupation weights w_i of the states.

In this approach, it is the high temperature of the electronic degrees of freedom that maintains the electron-hole plasma density. However, we note that the number of electrons in the conduction band will be dependent on the density of states near the chemical potential μ (and, similarly, the number of holes in the valence bands). For a given temperature, the electron-hole plasma density is much higher when the band gap is small than it is if the band gap is large. This is of great importance in the case of the Te A_1 phonon because, as we have seen in Sec. III, the band gap is strongly affected by the mode amplitude x. We discuss this point in more detail in Sec. VII.

B. Energy level filling for independent thermal distributions of electrons and holes

In the regime of slow electron-hole recombination, the ''hole state'' and ''electron state,'' electrons in the conduction and valence bands, respectively, are treated as distinct species. This distinction makes sense as long as the direct band gap remains substantial, as it does in tellurium when the A_1 phonon parameter x remains less than 1/3. The temperature and the electron-hole plasma density are now independent control variables in the calculation. Two chemical potentials are introduced, one for the conduction band states and one for the valence bands. Filling of each set of bands (conduction and valence) can be formally treated in almost exactly the same way as the single chemical potential problem, both sets of carriers occupying energy levels within their permitted bands and forming their own separate thermal distributions. We will assume that the temperature used in the filling of the conduction bands is the same as that used for valence bands, although it is not difficult to relax this constraint, if relevant.

To implement this model, the following procedure is carried out.

(i) For each Brillouin zone **k** point, the nine lowest-energy states, which correspond to the valence bands in the ground state, are labeled as ''hole states.'' The electrons remaining in these states following excitation are treated separately from the excited electrons in the conduction bands (10 and above). This is so, even if structural or electronic changes cause some former conduction-band electron state energy levels to be lowered below the upper hole-state energy levels at a different **k** point. Hole state electrons will not be permitted to occupy electron state energy levels, even if such occupation is energetically favorable.

(ii) All energy band levels higher than the first nine at each **k** point are labeled as ''electron states.'' Electrons fill these conduction-band states entirely separately from the hole states (valence bands).

(iii) The valence-band energy levels are filled with electrons according to a Fermi-Dirac distribution. This assumes that thermal equilibrium is established between carriers within the valence bands. The chemical potential μ_{h^+} used in filling these bands is determined by the condition that the total number of holes per unit volume equal the prescribed electron-hole plasma density, which is a control parameter for the calculation. The value of μ_{h^+} is found by the bisection method described in Sec. IV A.

(iv) The excited electrons are distributed among the conduction-band states according to a Fermi-Dirac distribution, with chemical potential μ_{e^-}. The value of μ_{e^-} is determined by the bisection method to satisfy the requirement that the density of excited electrons equal the prescribed electron-hole plasma density.

(v) Once the occupation weights w_i associated with all the single-particle states $\psi_i(\mathbf{r})$ are determined, the charge density of the excited system is calculated (as in the usual ground state calculations) by

$$\rho(\mathbf{r}) = \sum_i w_i |\psi_i(\mathbf{r})|^2, \tag{1}$$

where $\psi_i(\mathbf{r})$ is the value of the ith wave function at the position **r**.

(vi) The potential for the electrons for the next iteration of the self-consistent solution of the Kohn-Sham equation is determined from the charge density in Eq. (1).[24,11]

V. PHONON FREQUENCY CALCULATIONS

We calculate phonon frequencies using the ''frozen phonon'' technique.[11] The calculated structural energies at vari-

ous values of the phonon displacement x are fitted with a fifth-order polynomial $V(x)$. For large electron-hole densities, the initial amplitude of phonon motion is large enough that anharmonicity of the potential $V(x)$ may significantly affect the period of motion. Within the DECP mechanism, the starting point for the motion is x_{eq}^0, the equilibrium value of x when the electrons are in their ground state. The initial velocity is zero. The system then oscillates about x_{eq}, the new equilibrium value of x for the photoexcited system, with mode damping gradually reducing the amplitude of motion. To calculate the effects of anharmonicity, we have found the period of motion for the initial amplitude and for very small amplitude as follows: Energy conservation for the classical motion of the ions implies that the velocity $v(x)$ at phonon displacement x is given by

$$v(x) = \sqrt{\frac{2}{m}[V(x') - V(x)]}, \tag{2}$$

where m is the atomic mass and the classical turning point of the motion occurs at $x = x'$. The period of the initial amplitude motion is then given by

$$T = 2\int_{x_{eq}^0}^{x'} \frac{dx}{v(x)}, \tag{3}$$

where x' is the value of x on the opposite side of x_{eq} at which $V(x') = V(x_{eq}^0)$.

VI. TOTAL ENERGY CALCULATIONS

Calculations were performed using the plane-wave pseudopotential method[24,11] with the local density approximation (LDA) to exchange and correlation.[25] Plane waves up to energy cutoffs of 16 and 49 Ry were used in the expansion of the wave functions and charge density, respectively. We use semilocal pseudopotentials of *s*, *p*, and *d* symmetry, generated with an atomic reference configuration of $5s^{1.0}$, $5p^{4.0}$, and $5d^{0.5}$ using the method of Hamann, Schlüter, and Chiang.[23] Phonon frequencies were calculated by sampling the Brillouin zone with a uniform $10\times10\times10$ grid, centered at $\mathbf{k}=(0,0,0)$ (i.e., 124 **k** points in the irreducible zone), unless otherwise stated.

Temperature and Brillouin zone sampling

Due to the strong dependence of the phonon frequency on the character and filling of states near the Fermi level, it is necessary to sample a large number of points in the Brillouin zone to obtain a smooth variation of the energy as the phonon coordinate x varies. Figure 4 shows the calculated harmonic phonon frequency (see Sec. V) as a function of the carrier temperature, $\tau = k_B T$, for various levels of Brillouin zone sampling. The electron-hole plasma density is kept fixed (see Sec. IV B) at 1% of the valence electron density. It is found that above a certain temperature the frequency is essentially independent of both the level of sampling and the temperature but that at lower temperatures there is a large variation due to both.

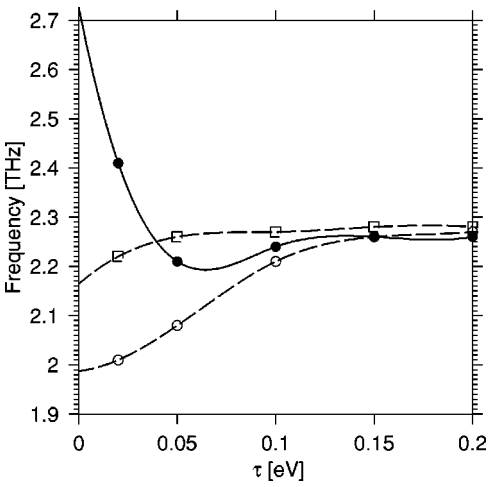

FIG. 4. Calculated A_1 phonon frequency as a function of the thermal energy, $\tau = k_B T$, used in the Fermi-Dirac distribution of the carriers, for a fixed electron-hole plasma density equal to 1% of the total valence electron density, showing the combined effects of electron temperature and Brilouin zone sampling. Brillouin zone sampling with grids of $8\times8\times8$ (solid circles), $9\times9\times9$ (open circles), and $10\times10\times10$ (squares) **k** points were used. The symbols indicate calculated values and the curves are polynomial fits to the calculated values shown.

The variation of the calculated frequency in Fig. 4 at low temperature is a numerical artifact of the finite sampling of the Brillouin zone and can be understood as follows: When a small number of **k** points is used, the weight associated with each individual state is relatively large. If a low-temperature Fermi-Dirac distribution is used, when the energy of a state crosses the Fermi level, the occupation w_i of the state changes abruptly, leading to an abrupt change in variation of the total energy. This severely affects the calculated phonon frequency in the frozen phonon method. Using a larger number of **k** points (thereby assigning less weight to any given state) or a larger temperature (allowing a smoother variation of the occupation for states near the Fermi energy) substantially reduces these abrupt changes. These combined effects of **k** point sampling and thermal broadening of the Fermi-Dirac distribution have been observed in other systems.[26] This effect is more severe for larger values of the electron-hole density.

Our conclusion from the analysis of combined effects of **k** point sampling and Fermi-Dirac distribution temperature on the calculated phonon frequencies is that the *true variation* (i.e., for infinite **k**-point sampling) *of the phonon frequency with electron-hole plasma temperature is negligible*. Once discontinuities due to finite sampling have been smoothed out, the phonon frequency shows a remarkable insensitivity to changes in temperature. Thus, any effects of rapid carrier cooling on the phonon dynamics will be relatively small. This insensitivity to electronic temperature also implies a general insensitivity of the frequency to details of the occupation of states within the low-lying conduction bands.

Thus, the effect of any slow intervalley carrier equilibration on the phonon frequency is negligible. For example, it can be seen from Fig. 3 that a change in electronic tempera-

ture τ from 0.1 eV to 0.2 eV gives rise to a substantial change in the weighting of occupation between the H and *A* points of the Brillouin zone. Nevertheless, we have seen that this change has a negligible effect on the phonon frequency when the Brillouin zone is fully sampled.

The use of the zero-temperature form of the LDA exchange and correlation potential to calculate the effects of exchange and correlation in the photoexcited system is not strictly justified since the eigenvalues calculated in this way are not the true quasiparticle excitation energies. However, the above discussion would suggest that it is only the gross features of the conduction bands that are important. Moreover, in this calculation the LDA gap (0.26 eV) is not too much different from the experimental band gap [0.33 eV Ref. 27)] and the band dispersions within the LDA conduction and valence bands are very similar to the experimentally determined dispersions.

Due to the subtle nature of the weak interchain interactions, the equilibrium structural parameters have been shown to be less accurate for Te than for systems such as silicon and diamond.[28,29] Most of our calculations are performed for experimental values of the lattice constants *a* and *c*. In order to check the validity of our use of the LDA band structure, we have calculated the frozen phonon frequencies at electron-hole plasma densities equal to zero and equal to 1% of the valence charge density, using the theoretical equilibrium lattice constants rather than the experimental values.[28] The phonon frequency and its derivative with respect to carrier density only change by 15%–20% when the theoretical lattice constants are used, despite substantial changes in the band gaps and in the details of the band dispersions. Our use of the LDA band structure is therefore justified by this insensitivity of the results to details of conduction-band dispersion and occupation at this level of accuracy.

VII. PHONON FREQUENCY SHIFT

We have calculated the excitation dependence of the A_1 phonon in two regimes of electron-hole recombination time: slow recombination, where conduction-band and valence-band carriers have separate chemical potentials, and fast recombination, where conduction-band and valence-band carriers share a common chemical potential.

A. Slow electron-hole recombination

Figure 5 shows the structural energy as a function of atomic displacement parameter *x* for excited carrier densities, ranging from 0% to 1.25% of the valence electron density. The lattice constants are fixed at their experimental values. In each case the temperature used in the Fermi-Dirac distribution function was $\tau = 0.05$ eV. (We note that this temperature is substantially smaller than the initial experimental temperature of 0.4 eV, which one would expect for photon energies of 1.5 eV. However, as already discussed, the carrier temperature has little effect on the phonon dynamics.) The ground-state equilibrium value of *x* is found to be 0.2686, approximately 2% larger than the experimental value of 0.2633. The frequency of oscillation about this minimum

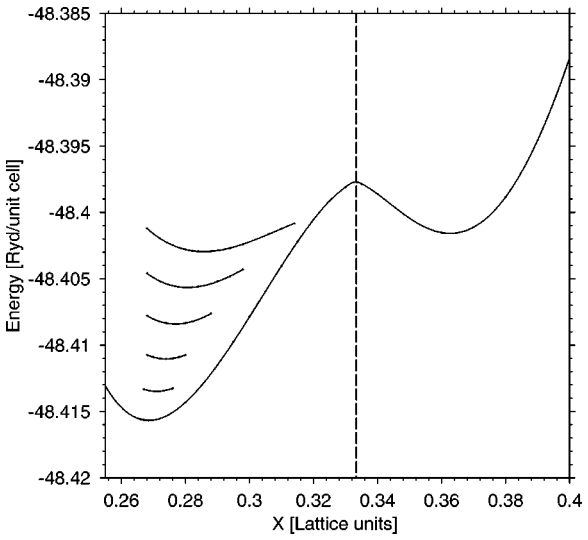

FIG. 5. Total energy per unit cell as a function of phonon coordinate *x* for photoexcited plasma densities equal to 0% (lowermost curve), 0.25%, 0.5%, 0.75%, 1.0%, and 1.25% (uppermost curve) of the valence electron density. The vertical dashed line indicates the value of $x = \frac{1}{3}$ corresponding to the high-symmetry γ-Te structure. The curves are cubic spline fits through the calculated energies.

was calculated as 3.24 THz, 10% smaller than the value of 3.6 THz obtained in conventional Raman scattering.[15]

For the ground-state curve there are two minima, corresponding to the equilibrium $x < \frac{1}{3}$ and $x > \frac{1}{3}$ structures which may be viewed as Peierls distortions of the $x = \frac{1}{3}$ (γ-Te) structure, as discussed in Sec. III. (We note that the $x > \frac{1}{3}$ structure is not stable, since a small clockwise rotation of every second helix of atoms indicated in Fig. 2 brings the structure back to the α-Te structure with $x < \frac{1}{3}$.) For $x < \frac{1}{3}$, the atomic forces contributed by the valence-band states tend to restore the equilibrium at $x = 0.2686$ and the conduction-band states tend to force the structure towards $x = 0.364$. (For $x > \frac{1}{3}$, the roles of valence and conduction bands are reversed — see discussion of charge densities, below.) Thus, as the electron-hole plasma density increases, the balance between the conduction-band and valence-band forces changes and the equilibrium value of *x* increases.

In Fig. 5 one can see a broadening of the curves near the minima and an increase in x_{eq} as the excited-carrier density increases. This is shown more clearly in Fig. 6(a). It is this change in x_{eq} which is responsible for the DECP mechanism. In each of the excited-state curves of Fig. 5, we have shown that portion of the energy versus *x* curve which would be traversed by the photoexcited system if the motion were undamped. This is the initial amplitude of motion, for which the frequency is shown in Fig. 6(b). Damping of the phonon motion will result in a decrease of the amplitudes of successive cycles of the oscillation from the maximum value of $|x_{eq}^0 - x_{eq}|$ to 0.

It is found that an indirect closing of the band gap occurs at $x = 0.286$, with the energy states at H raising slightly above those at *A*. A direct crossing of energy bands does not occur until the bands become degenerate at $x = \frac{1}{3}$. This clos-

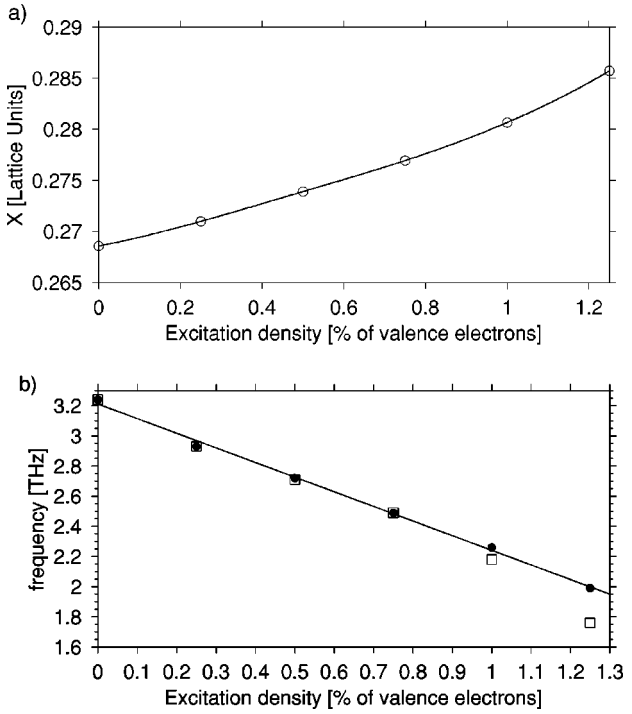

FIG. 6. (a) Equilibrium atomic displacement parameter and (b) A_1 phonon frequency vs photoexcited carrier density for the two chemical potential model (see Sec. IV A). The curve in (a) is a cubic spline fit through the calculated points. The frequency in (b) is shown for the initial DECP amplitude motion (open squares) and for the final, small amplitude motion (solid circles). The slope of the linear fit to the small amplitude frequencies in (b) corresponds to a frequency shift of -0.97 THz for 1% of the valence electrons excited into the conduction bands.

ing of the indirect band gap is only relevant for our calculations for excitation densities greater than 1% of valence electrons. At 1.25% excitation the maximum time spent during an oscillation with $x>0.286$ is less than 0.25 ps per cycle and, since the relaxation time for carriers from former valence states to former excited states with phonon emission is likely to be of the order of 1–2 ps, we have not allowed for any phonon-assisted electron-hole recombination during this time.

From each fitted curve of the total energy versus x, we have calculated the maximum and minimum amplitude phonon frequencies as a function of photoexcited carrier density, using the frozen phonon method described in Sec. V. The results are presented in Fig. 6(b). The graph shows an approximately linear decrease in phonon frequency with increasing excitation density. The anharmonicity of the curves has a significant effect on the frequency at maximum amplitude only for excitation densities greater than 1% of the valence electrons.

To examine the real-space character of conduction and valence bands and the associated forces on the atoms of each helix in the α-Te structure, we have calculated the charge densities associated with various electronic bands near the Fermi level. Figure 7 shows that the electron states which form the highest valence bands when $x<\frac{1}{3}$ (upper left panel) correspond quite closely to those that form the lowest conduction bands when $x>\frac{1}{3}$ (lower right panel). Conversely, the electron states which form the lowest conduction bands when $x<\frac{1}{3}$ (upper right panel) correspond to those that form the highest valence bands when $x>\frac{1}{3}$ (lower left panel). The conduction and valence states shown become degenerate at $x=\frac{1}{3}$ and cross one another at this point. This means that an excitation of electrons into the conduction band when $x<\frac{1}{3}$ is an excitation of electrons into states which favor the $x>\frac{1}{3}$ structure. The system is therefore pushed in this direction and the helical radius increases. The excitation of electrons into the conduction band corresponds to a placement of electrons into the center of the helices where the electron density is highest, thereby pushing the helices apart. The higher the level of electronic excitation, the greater the influence of the $x>\frac{1}{3}$ structure.

B. Fast electron-hole recombination

Figure 8 shows the temperature dependence of x_{eq} and phonon frequency for the single chemical potential model. The behavior is qualitatively different from the two-chemical-potential model and contrary to experiment.[15] In this case the α-Te helical structure seems to be strengthened by the high electron temperature. The closing band gap and changing density of states near the Fermi level as x is increased means that the number of electrons in the conduction band changes during the motion. This contributes an effective binding force to the helices since the electronic energy can be lowered by a reduction of the density of states near the Fermi level. This is illustrated in Fig. 9: the percentage of electrons occupying excited states is at a maximum for the metallic γ-Te structure and decreases again as the bands begin to recede from the Fermi level beyond $x=\frac{1}{3}$. In the two-chemical-potential model, the effect of a changing density of states is simply a movement of the chemical potentials. For example, at 1% excitation the hole-state chemical potential increases from 8.57 eV at $x=0.2686$ to 8.71 eV at $x=0.294$ while the electron-state chemical potential decreases from 9.53 eV to 9.29 eV over the same range.

From this it is clear that, if one is to model the effects of short-time-scale electronic excitation of the ion dynamics in systems where electron-hole recombination is sufficiently slow, an assumption of thermal and chemical equilibrium within all electronic bands may lead to qualitatively incorrect results. This opens the question of how one may more generally allow for the dynamical redistribution of electrons among the states in a photoexcited system. Neither of the methods used here strictly follows the evolution of the electronic distribution, though it is clear that the method of slow electron-hole recombination and rapid thermalization within each band provides a better representation of the phonon dynamics in photoexcited tellurium.

VIII. REFLECTIVITY OSCILLATIONS

A. Physical model and numerical methods

In order to use the calculated results for the phonon frequency shift as a function of electron-hole plasma density to predict the expected reflectivity oscillations, several physical

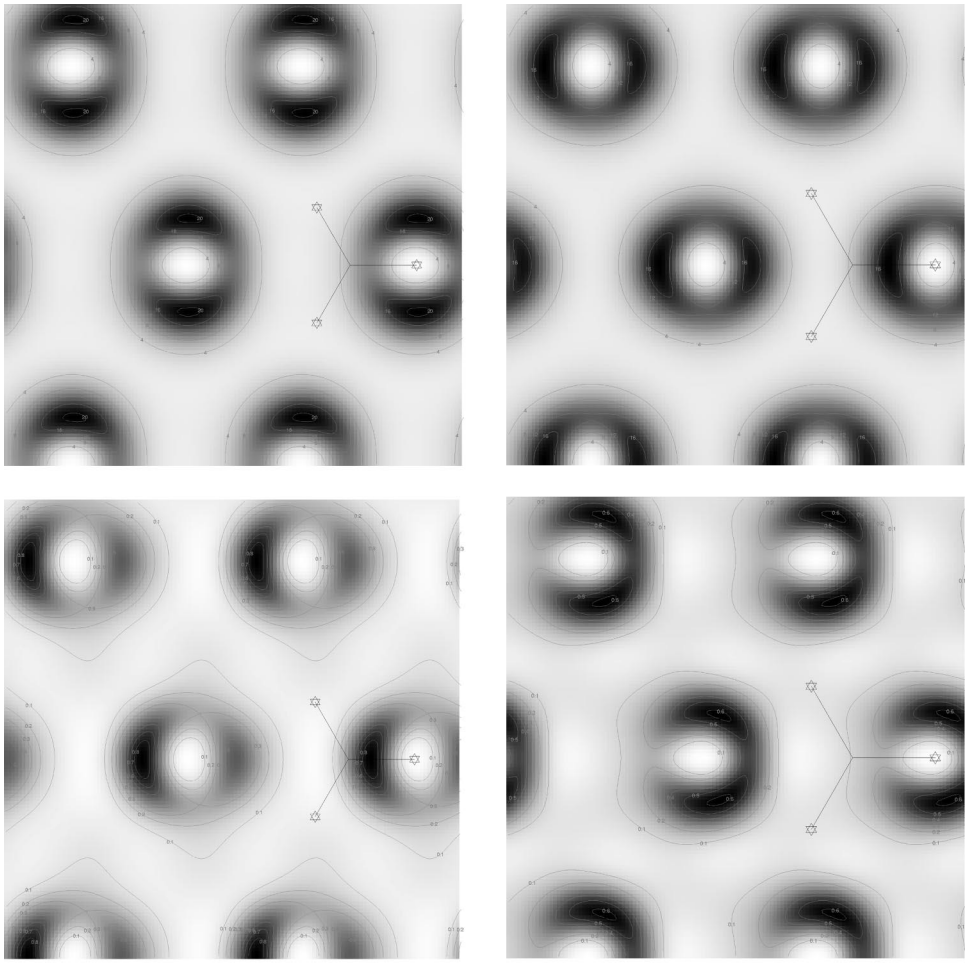

FIG. 7. Cumulative electron density from selected bands near the Fermi energy for structures with atomic displacement $x<\frac{1}{3}$ (upper panels) and $x>\frac{1}{3}$ (lower panels). The densities shown are for electrons occupying: the highest three valence bands for $x=0.29$ (upper left panel), the lowest three conduction bands for $x=0.29$ (upper right panel), the highest three valence bands for $x=0.36$ (lower left panel), and the lowest three conduction bands for $x=0.36$ (lower right panel). The plane of the plots is that which passes through the center of one of the atoms and is perpendicular to the c axis. The positions in the (a_1,a_2) plane of the atoms for one of the $x<\frac{1}{3}$ helices are indicated by stars. Dark regions correspond to regions of high electron density. In each plot the separation between contours and the density range corresponding to the white-black spectrum are different.

processes occuring in the pump-probe experiments must be taken into consideration: (i) generation of electron-hole pairs by photons absorbed from the pump pulse; (ii) diffusion of carriers; (iii) phonon dynamics driven by carrier densities at each depth, according to the parameters calculated above; (iv) dependence of the dielectric function $(\epsilon_1+i\epsilon_2)\epsilon_0$ on phonon displacement and carrier density; and (v) reflection of the probe pulse from the medium, where the dielectric function $\epsilon(z,t)\epsilon_0$ depends on depth z and time t. Since the laser pump focus is of the order of 100 μm, whereas all relevant processes occur within approximately 100 nm of the surface, variations of the plasma density and related quantities in directions parallel to the surface can be neglected in treating these effects.

To calculate both the probe reflectivity and the pump electron-hole pair production, we must find the radiation fields within the material at each time t. We will assume that the radiation is incident normal to the surface and has electric polarization in the x direction. The electromagnetic fields $E(z,t)\exp(-i\omega t)$ and $H(z,t)\exp(-i\omega t)$ in the material then satisfy the Maxwell equations

$$\frac{dH}{dz}=i\omega\epsilon(z,t)\epsilon_0 E, \quad \frac{dE}{dz}=i\omega\mu_0 H, \tag{4}$$

where we have ignored propagation delay effects by neglecting time derivatives of the field amplitudes $E(z,t)$ and $H(z,t)$ and of the dielectric function ϵ. Rewriting the fields as $E=(y_1+iy_2)/\sqrt{\epsilon_0}$ and $H=(y_3+iy_4)/\sqrt{\mu_0}$, we obtain four coupled equations for the real fields:

$$\frac{dy_1}{dz}=-k_0 y_4,$$

$$\frac{dy_2}{dz}=k_0 y_3,$$

$$\frac{dy_3}{dz}=-k_0(\epsilon_2 y_1+\epsilon_1 y_2),$$

$$\frac{dy_4}{dz}=k_0(\epsilon_1 y_1-\epsilon_2 y_2), \tag{5}$$

where k_0 is the radiation wave number in vacuum. These equations can be solved numerically by integration from deep in the bulk out to the surface, using a standard fourth-order Runge-Kutta integration scheme.[31] We impose the boundary condition that the asymptotic fields at large depth be for a wave decaying in amplitude into the bulk, which is satisfied if $y_2=0$, $y_3=n_1 y_1$, and $y_4=n_2 y_1$ as $z\to\infty$, where $n=\sqrt{\epsilon}=n_1+in_2$ is the complex refractive index of the unperturbed material. The reflectivity R may be found by

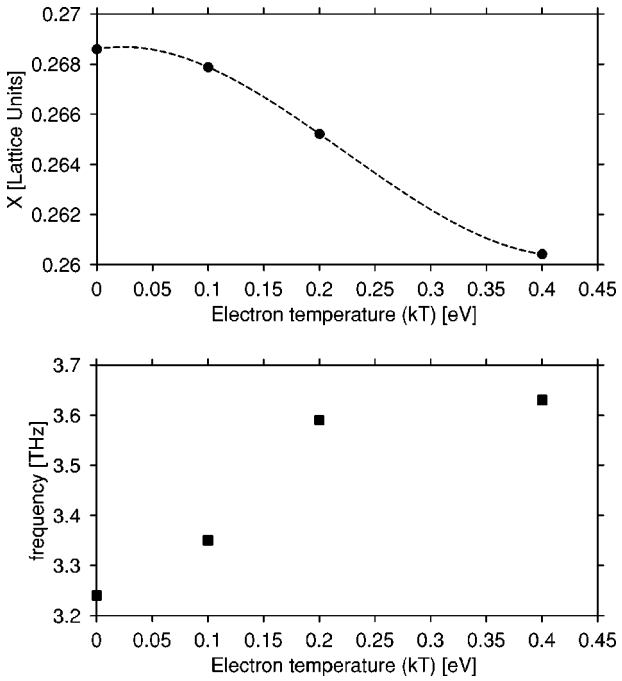

FIG. 8. (a) Equilibrium atomic displacement parameter and (b) A_1 phonon frequency vs temperature for the single-chemical-potential model (see Sec. IV A). The curve in (a) is a cubic spline fit through the calculated points. The frequency in (b) is shown for the initial DECP amplitude motion.

matching the radiation fields at the surface of the material to incident and reflected waves in the vacuum, giving

$$2E_{\rm inc}=(y_1+y_3)+i(y_2+y_4),$$

$$2E_{\rm ref}=(y_1-y_3)+i(y_2-y_4), \tag{6}$$

at $z=0$ and $R=|E_{\rm inc}/E_{\rm ref}|^2$. We use an integration step of 1 nm in the Runge-Kutta scheme and a maximum integration depth of 1 μm.

Photon absorption from the pump pulse is determined by the imaginary part $\epsilon_2(z)$ of the dielectric constant. Assuming linear absorption of photons, the rate of change of the electron-hole density $n(z,t)$ is given by

$$\frac{\partial n}{\partial t}=-\frac{1}{\hbar\omega}\frac{\partial S}{\partial z}, \tag{7}$$

where $S=c(y_1y_3+y_2y_4)$ is the radiation energy flux. The amplitude of the asymptotic field $y_1(z)$ at large z is scaled, so that the fields at the surface match those in vacuum for a given intensity of the incident radiation. The pump pulse is assumed to have a negligible rise time and a constant intensity for its entire duration, so that the radiation energy flux incident on the surface is assumed to be equal to the pump fluence divided by the pulse time for the duration of the pump pulse. After application of the pump pulse, the generation of electron-hole pairs ceases (i.e., S is negligible) and the total number of electron-hole pairs is assumed to remain constant.

So far, we have not considered the effects of carrier diffusion. However, because of the relatively short absorption depth of radiation in the incident laser pump pulse, the initial electron-hole plasma density decreases rapidly with depth below the sample surface. Carrier diffusion then leads to a rapid decay of the plasma density at the surface within a few cycles of the A_1 phonon. This may be accounted for by the addition of a diffusion term in the time derivative of the carrier density:

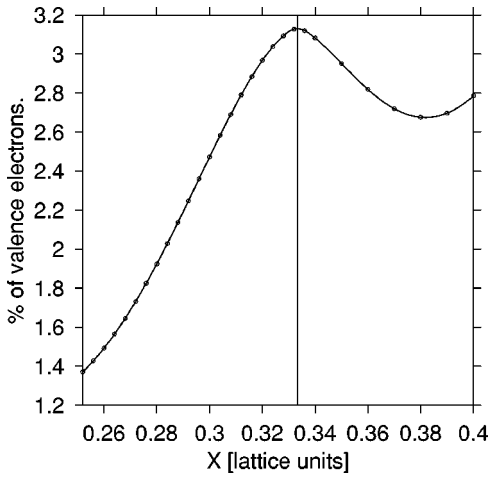

FIG. 9. The fraction of the valence electrons which occupy the conduction band as a function of atomic displacement x at a temperature of $\tau=0.4$ eV for the single-chemical-potential model.

$$\frac{\partial n(z,t)}{\partial t}=D\nabla^2 n(z,t)-\frac{1}{\hbar\omega}\frac{\partial S}{\partial z}, \tag{8}$$

where D is the ambipolar diffusion constant and S is nonzero only during application of the pump pulse. The equilibrium ambipolar diffusion constant in Te is 40 cm^2 s^{-1}.[30] For the highly excited carrier distribution initially created after the incidence of the pump pulse, the value of D may be different from its equilibrium value, but we would expect it to be of the same order of magnitude. (As we shall see below, comparison of our simulations with experimental results for reflectivity oscillations will allow us to obtain quite an accurate estimate of D for this system.) The evolution of the density due to diffusion is solved by the Crank-Nicholson method.[31]

The phonon displacement $x_{\rm ph}(z,t)$ is driven by the carrier plasma density $n(z,t)$. The equilibrium position x_0 and vibration frequency ω_0 depend on n, as shown in Fig. 6. The equation of motion for the phonon displacement $x_{\rm ph}(z,t)$ is then given by

$$\frac{\partial^2 x_{\rm ph}}{\partial t^2}=-\omega_0(n)^2[x_{\rm ph}-x_0(n)]-\gamma\frac{\partial x_{\rm ph}}{\partial t}, \tag{9}$$

where we have introduced the phenomenological damping force $-\gamma\partial x_{\rm ph}/\partial t$ to allow for homogeneous broadening of the phonon line. For small plasma density, we may use a linear approximation: $x_0(n)=\overline{x_0}+(\partial x_0/\partial n)n$ and $\omega_0(n)=(\overline{\omega_0}+\partial\omega_0/\partial n)n$. Values of $(\partial x_0/\partial n)=7.4\times10^{-24}$ cm^3 and $\partial\omega_0/\partial n=-3.45\times10^{-21}$ THz cm^3 give good linear fits to the results shown in Fig. 6. (Note that 1% of the valence density in tellurium is 1.766×10^{21} cm^{-3}.) We use the ex-

perimental value (3.6 THz) for the unperturbed phonon frequency, giving $\bar{\omega}_0 = 22.6\ \mathrm{s}^{-1}$. The integration of Eq. (9) is performed by a modification of the standard leapfrog approach[32] for systems with damping, using the value of $\gamma = 2/\tau = 1.1\times 10^{12}\ \mathrm{s}^{-1}$, where τ is the dephasing time which is compatible with the attenuation observed in low-fluence experiments (see Fig. 5 of Ref. 15). The integration time-step used was 2 fs for all dynamical aspects of the simulations. The dynamics of the system was simulated for a total time of 10 ps.

The dielectric constant at each depth is influenced by the phonon displacement x_{ph} and the carrier density n at that depth. Since ϵ_1 is much larger than ϵ_2, changes in ϵ_1 have a larger effect on the optical reflectivity. Saturation effects in the absorption of photons from the pump pulse are not taken into account, limiting the applicability of our results to pump fluences substantially less than 3 mJ/cm^2 for a 100 fs pump pulse.[15] Thus, in modeling the reflectivity oscillations, we will assume for simplicity that ϵ_2 remains unchanged and

$$\epsilon_1 = \bar{\epsilon}_1 + \frac{\partial \epsilon_1}{\partial x_{\mathrm{ph}}} x_{\mathrm{ph}} + \frac{\partial \epsilon_1}{\partial n} n, \tag{10}$$

where $\bar{\epsilon}_1$ is the real part of the dielectric constant for the unperturbed material. We take values of $\bar{\epsilon}_1 = 32$ and $\epsilon_2 = 11$ for 825 nm radiation from the literature.[33] The derivatives $\partial\epsilon_1/\partial x_{\mathrm{ph}}$ and $\partial\epsilon_1/\partial n$ are taken as adjustable parameters, which will be used to fit the amplitude of the experimentally observed background shift and initial oscillations in the reflectivity. These parameters influence primarily the overall scale of the reflectivity oscillations, rather than their frequency spectrum, and the dependence of the frequency peak on pump fluence is not strongly affected by their values.

In pump-probe experiments, the reflectivity measured is an average over the duration of the probe pulse. In our simulations we then take a running average of the reflectivity over a time window equal to the probe pulse width, which is taken to be 100 fs, the same as the pump pulse. The final results for the reflectivity are only slightly different from those obtained using the instantaneous reflectivity.

B. Comparison with pump-probe experiments

Because we have not allowed for saturation effects in our simulations, we use the low-fluence data reported in Fig. 4 of Ref. 15 and Fig. 2 of Ref. 16 for comparison with our simulations. In Fig. 4 of Ref. 15, the frequency shift is shown as a function of the initial background reflectivity change ΔR_{bg}. The slope of the data is $d\nu/d\Delta R_{\mathrm{bg}} = -0.064$ THz per 1% change in initial background reflectivity. On the other hand, Fig. 2 of Ref. 16 shows the frequency shift (for a somewhat wider range of pump fluences) as a function of an excitation density parameter N_{exc}. This excitation density was determined from the pump fluence, assuming exponential absorption of photons in an absorption depth of 50 nm. Thus, N_{exc} corresponds directly to the pump fluence F, with $F = 2.15 N_{\mathrm{exc}}$, where N_{exc} is in units of 10^{21} cm^{-3} and F is in mJ/cm^2. The slope of the data over the range shown in Fig. 2 of Ref. 16 is $d\nu/dF = -0.058$ THz per mJ/cm^2.

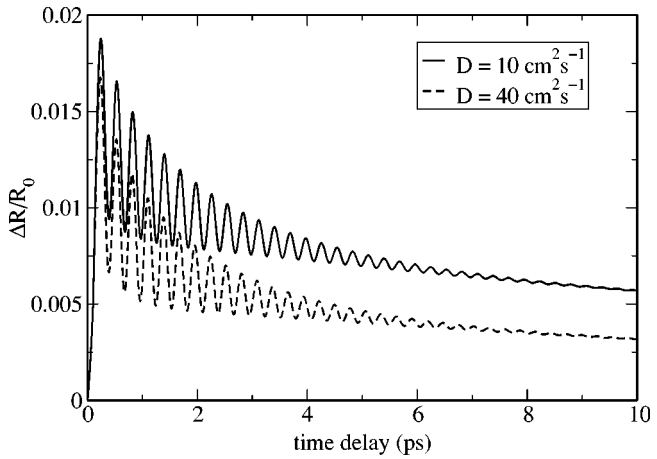

FIG. 10. Simulated pump-probe reflectivity oscillations in tellurium for a pump fluence of 1.19 mJ cm^{-2}. The parameters $\partial\epsilon_1/\partial x_{\mathrm{ph}} = 3.5\times 10^2$, $\partial\epsilon_1/\partial n = 2.75\times 10^{-21}$ cm^{-3}, and $D = 10$ cm^2/s were chosen to match the experimental results, as discussed in the text. The reflectivity for $D = 40$ cm^2/s is shown for comparison.

However, saturation of absorption affects the data at the higher end of this range; fitting only data in the low-fluence regime ($N_{\mathrm{exc}} < 1.5\times 10^{21}$ cm^{-3}, where the frequencies vary over the same range as in Fig. 4 of Ref. 15) gives a slope $d\nu/dF = -0.07$ THz per mJ/cm^2. This is a slightly larger slope than is indicated for data over the much larger range of pump fluences presented in Fig. 3 of Ref. 15, where saturation of absorption is a major factor, but is consistent with the data for low-fluence ($F \leqslant 2.4$ mJ/cm^2) included there. Thus, we can associate initial background reflectivity changes (in %) with pump fluence (in mJ/cm^2) for the low fluence regime through the relation $\Delta R_{\mathrm{bg}} = (0.07/0.064)F = 1.09F$.

Estimating the initial background reflectivity to be 1.3% for the prepump signal of the inset to Fig. 4 of Ref. 15, we can infer that the fluence for this pump pulse was 1.3/1.09 $= 1.19$ mJ/cm^2 and compare the main features of the reflectivity signal with the corresponding results of our simulations for a pump fluence of 1.19 mJ/cm^2, as shown in Fig. 10. This allows us to estimate values for $\partial\epsilon_1/\partial x_{\mathrm{ph}}$, $\partial\epsilon_1/\partial n$, and the diffusion constant D. Our simulations give an initial background change, initial oscillation amplitude, and decay of the background reflectivity over 6 ps in good agreement with the experimental data when we use values of $\partial\epsilon_1/\partial x_{\mathrm{ph}} = 3.5\times 10^2$, $\partial\epsilon_1/\partial n = 2.75\times 10^{-21}$ cm^{-3}, and $D = 10$ cm^2/s. We note that using the standard equilibrium value of $D = 40$ cm^2/s gives a decay of the background reflectivity which is substantially more rapid than that observed in the experiments.

Using these parameters in our model, we then find a peak in the frequency at $\nu_{max} = 3.515$ THz for a pump fluence $F = 1$ mJ/cm^2. This gives a variation of the peak frequency, $d\nu/dF = -0.085$ THz per mJ/cm^2, in very good agreement with the low-fluence data. The values of the fitted parameters $\partial\epsilon_1/\partial x_{\mathrm{ph}}$ and $\partial\epsilon_1/\partial n$ used in the simulation have a very small effect on the value of $d\nu/dF$. The value used for the diffusion constant has a noticeable effect; for example, using

the standard equilibrium value[30] $D=40$ cm^2/s in the simulations gives a value $d\nu/dF=-0.055$ THz per mJ/cm^2.

We have not included saturation effects on the production of electron-hole pairs and so we cannot sensibly compare our results with experiment at high fluences. We expect optical saturation effects in the real material, which become very noticeable for fluences above 3 mJ/cm^2, to reduce slightly the variation of the peak frequency with pump fluence in the low-fluence regime because of the smaller density of electron-hole pairs produced at the surface.

A greatly increased damping of reflectivity oscillations is observed in the experiments involving high pump fluences. On the basis of double-pump experiments, it was proposed[15] that this was due to the large inhomogeneity of the initial plasma density within the optical absorption depth. However, in our simulations, we see that variation of the electron-hole density with depth (and the associated inhomogeneous broadening of the phonon oscillations) does *not* give rise to a large damping of the reflectivity oscillations. We see a slight increase in damping of the reflectivity oscillations in simulations for high fluences, but nothing like the kind of damping shown in Fig. 1 of Ref. 15. The simulations would seem to suggest that some other physical mechanisms, beyond what is in our model, come into play at high fluences.

IX. DISCUSSION AND CONCLUSIONS

We have demonstrated how photoinduced changes in electronic structure can dramatically alter the forces between ions and produce a coherent phonon motion in materials, such as tellurium, with an A_1 phonon mode. The phonon frequency decreases approximately linearly and the initial amplitude of the phonon increases with the strength of the carrier excitation. We have calculated the dependence of the phonon frequency and initial coherent phonon amplitude on carrier plasma density, allowing comparison with the laser excitation experiments and a quantitative estimate of the surface carrier density from the measured A_1 phonon frequency.

Experiment[15] finds a relaxation with time of both frequency and amplitude back towards their values in the unexcited system. This can be explained from the results shown above by two effects: (i) damping of the phonon amplitude, which leads to a lessening of the anharmonic frequency shift, thereby increasing the frequency with successive cycles of the motion [see Fig. 6(a)]; (ii) a continuous reduction of the surface carrier density by diffusion normal to the surface. We find the anharmonicity has a relatively small effect and may be neglected for carrier plasma densities less than 1% of the valence electron density and that the dominant effect in the experiments of Hunsche *et al.*[15] probably arises from carrier diffusion normal to the surface.

Direct quantitative comparison of simulations of the reflectivity shows a good agreement with the experimental data for low-fluences. In particular, we estimate the derivative of the frequency of reflectivity oscillations with respect to pump fluence to be $d\nu/dF=-0.085$ THz per mJ/cm^2, in very good agreement with the experimental result $d\nu/dF=-0.07$ THz per mJ/cm^2 for low fluence data. Comparing the decay of the background reflectivity seen in our simulations with corresponding experimental results allows an accurate determination of the ambipolar diffusion constant $D=10$ cm^2/s in the highly excited regime, substantially smaller than its equilibrium value $D=40$ cm^2/s.

At high pump fluences, where optical saturation becomes important, the results of the simulations differ from the experimental observations. In particular, we find much less broadening of the frequency peaks of the reflectivity oscillation than is found in experiment. Further developments of the model used here for the coupled dynamics of carriers, phonons, and radiation are required to describe this regime.

From the point of view of simulations of photoexcited materials using *ab initio* methods based on DFT, a very important result of this study is the demonstrated discrepancy between calculations based on fast electron-hole recombination and those based on slow recombination. Simulations based on a single thermal distribution of electrons in all bands[7–9] implicitly assume very fast electron-hole recombination and may not provide an adequate representation of the phonon dynamics on the picosecond time scale.

This work was supported by Forbairt Contract No. SC/96/742 and by the Irish Higher Education Authority Program for Research in Third Level Institutions.

[1] Jagdeep Shah, *Ultrafast Spectroscopy of Semiconductors and Semiconductor Nanostructures*, Springer Series in Solid State Sciences, Vol. 115 (Springer, New York, 1996).
[2] R. Merlin, Solid State Commun. **102**, 207 (1997).
[3] H. J. Zeiger, J. Vidal, T. K. Cheng, E. P. Ippen, G. Dresselhaus, and M. S. Dresselhaus, Phys. Rev. B **45**, 769 (1992).
[4] J. A. Van Vechten, R. Tsu, and F. W. Saris, Phys. Lett. **74A**, 417 (1979).
[5] S. Fahy and R. Merlin, Phys. Rev. Lett. **73**, 1122 (1994).
[6] P. Saeta, J.-K. Wang, Y. Siegal, N. Bloembergen, and E. Mazur, Phys. Rev. Lett. **67**, 1023 (1991).
[7] R. Biswas and V. Ambegaokar, Phys. Rev. B **26**, 1980 (1982); Phys. Rev. Lett. **50**, 285 (1983).
[8] P. Stampfli and K. H. Bennemann, Phys. Rev. B **42**, 7163 (1990); **46**, 10 686 (1992); **49**, 7299 (1994).
[9] P. L. Silvestrelli, A. Alavi, M. Parrinello, and D. Frenkel, Phys. Rev. Lett. **77**, 3149 (1996); Phys. Rev. B **56**, 3806 (1997).
[10] P. Hohenberg and W. Kohn, Phys. Rev. **136**, B864 (1964); W. Kohn and L. J. Sham, Phys. Rev. **140**, A1133 (1965).
[11] W. E. Pickett, Comput. Phys. Rep. **9**, 115 (1989).
[12] M. C. Payne, M. P. Teter, D. C. Allan, T. A. Arias, and J. D. Joannopoulos, Rev. Mod. Phys. **64**, 1045 (1992).
[13] M. Parrinello, Solid State Commun. **102**, 107 (1997).
[14] A. Alavi, J. Kohanoff, M. Parrinello, and D. Frenkel, Phys. Rev. Lett. **73**, 2599 (1994).
[15] S. Hunsche, K. Wienecke, T. Dekorsy, and H. Kurz, Phys. Rev. Lett. **75**, 1815 (1995).
[16] S. Hunsche, K. Wienecke, and H. Kurz, Appl. Phys. A: Mater.

Sci. Process. **62**, 499 (1996).
[17] P. Tangney and S. Fahy, Phys. Rev. Lett. **82**, 4340 (1999).
[18] G. McMahan, R. H. Martin, and S. Satpathy, Phys. Rev. B **38**, 6650 (1989); M. S. Hybertsen, M. Schlüter, and N. E. Christensen, *ibid.* **39**, 9028 (1989).
[19] W. Z. Lin, J. G. Fujimoto, E. P. Ippen, and R. A. Logan, Appl. Phys. Lett. **50**, 124 (1987); **51**, 161 (1987); W. Z. Lin, R. W. Schoelein, J. G. Fujimoto, and E. P. Ippen, IEEE J. Quantum Electron. **QE-24**, 267 (1988).
[20] M. Rasolt, Phys. Rev. B **33**, 1166 (1986).
[21] C. Kittel and H. Kroemer, *Thermal Physics* (Freeman, New York, 1980), pp. 432–435.
[22] Jerry Donohue, *The Structures of the Elements* (Wiley Interscience, New York, 1974).
[23] D. R. Hamann, M. Schluter, and C. Chiang, Phys. Rev. Lett. **43**, 1494 (1979).
[24] J. Ihm, A. Zunger, and M. L. Cohen, J. Phys. C **4**, 4409 (1979).
[25] J. P. Perdew and A. Zunger, Phys. Rev. B **23**, 5048 (1981).
[26] M. J. Gillan, J. Phys.: Condens. Matter **1**, 689 (1989).
[27] V. B. Anzin, M. I. Eremets, Yu. V. Kosichkin, A. I. Nadezhdinskii, and A. M. Shirokov, Phys. Status Solidi A **42**, 385 (1977).
[28] F. Kirchhoff, N. Binggeli, G. Galli, and S. Massida, Phys. Rev. B **50**, 9063 (1994), and references therein.
[29] G. Kresse, J. Furthmüller, and J. Hafner, Phys. Rev. B **50**, 13 181 (1994).
[30] P. Grosse and W. Richter, in *Physics of Non-tetrahedrally Bonded Elements and Binary Compounds*, edited by O. Madelung, Landolt-Börnstein, New Series, Group III, Vol. 17, Pt. e (Springer, Berlin, 1983).
[31] W. H. Press, B. P. Flannery, S. A. Teukolsky, and W. T. Vetterling, *Numerical Recipes* (Cambridge University Press, Cambridge, England, 1989).
[32] S. Fahy, S. Twohig, M. Stefansson, and D. Courtney, Phys. Rev. E **57**, 2799 (1998).
[33] E. D. Palik, in *Handbook of Optical Constants of Solids*, edited by E. D. Palik (Academic Press, New York, 1997), Vol. II.